Research Article

Yang Guo*, Kehua Tan, Xiaoying Guo*, Huirong Li, and Xian Jian

Multi-core/shell SiO₂@Al₂O₃ nanostructures deposited on Ti₃AlC₂ to enhance high-temperature stability and microwave absorption properties

https://doi.org/10.1515/ntrev-2022-0545 received January 28, 2023; accepted April 5, 2023

Abstract: Poor high-temperature stability (HTS) and weak microwave absorption performance (MAP) are a major restriction for wave-absorbing materials in elevated temperature ambient. Consequently, the Stöber process and the sol-gel method are first devised and used to create multi-core/shell SiO₂@Al₂O₃ nanostructures (MCSNs) on Ti₃AlC₂ (TAC). The MCSNs with a thickness of 135–215 nm raise the starting oxidation temperature of the matrix by 400°C. Furthermore, the weight gain drops from 17.44 to 2.32% within 1 h at 800°C. The effective absorption bandwidth with a reflection loss (RL) $\leq -10 \, dB$ of the MCSNscoated TAC is 3.25 GHz (8.68-11.27 and 11.63-12.29 GHz) at a thickness of 2.0 mm, which is 4.7 times that of the matrix. The minimum RL is reduced by a factor of 2.77 from -10.68 to -29.55 dB. The enhanced MAP is due to the introduced multiple reflection events and scattering mechanism as well as the enhanced electronic polarization, interface polarization, and polarization relaxation. The growth of the MCSNs provides a reference for the design and preparation of bifunctional materials with good HTS and MAP.

Keywords: Ti₃AlC₂, multi-core/shell SiO₂@Al₂O₃ nanostructures, high-temperature stability, microwave absorption properties

Kehua Tan, Huirong Li: School of Electrical and Information Engineering, University of Panzhihua, Panzhihua 617000, China Xian Jian: School of Materials and Energy, University of Electronic Science and Technology of China, Chengdu, 611731, China

1 Introduction

The extreme electromagnetic environment (including high temperature, high damp heat, and salt fog) have brought high-temperature (>300°C), oxidation-resistant microwave absorbing materials (MAMs) into focus [1-4]. These materials can be used in civil, military, and aerospace equipment (such as for the nozzle, heat shield, and nose cone) [5-8]. Therefore, materials with outstanding high-temperature stability (HTS) and microwave absorption performance (MAP) are widely studied [9,10]. In order to meet these requirements, various MAMs have been developed, mainly including magnetic materials (such as magnetic metals [11,12] and ferrites [13]), carbon-based materials (such as carbon nanotubes [14,15], carbon fibers [16], and graphene [5]), and ceramic-based materials (such as SiC_{np}/C_f [17], PyC-SiC_f/SiC [18], and C_f /SiC_{nw} [19]). The general use of magnetic materials in high-temperature situations is severely constrained by the low Curie temperature [20]. Furthermore, once the temperature reaches 300°C, carbonbased materials begin to oxidize [21]. Naturally, SiC-based materials with good HTS and chemical stability become one of the best choice for high-temperature MAMs [22]. However, the low carrier concentration and single polarization mechanism prevent SiC from achieving excellent MAP.

Until now, the introduction of dielectric materials to tune the complex permittivity and polarization mechanism of SiC-based materials has been a commonly used strategy to improve their MAP [18,23]. Han *et al.* prepared SiC nanowires reinforced SiC_f/SiC composites *via* chemical vapor infiltration [24]. The conductivity and complex permittivity of the composites showed a significant uplift dependence on temperature. Furthermore, the minimum reflection loss (RL_{min}) was $-47.5\,\mathrm{dB}$ at a thickness of 2.5 mm at 11.4 GHz and 600°C, and the effective absorption bandwidth (EAB; RL $\leq -10\,\mathrm{dB}$) was 2.8 GHz. Huo *et al.* prepared heterogeneous SiC/ZrC/SiZrOC hybrid nanofibers containing different

^{*} Corresponding author: Yang Guo, School of Electrical and Information Engineering, University of Panzhihua, Panzhihua 617000, China, e-mail: guoyangchn@126.com

^{*} Corresponding author: Xiaoying Guo, School of Electrical and Information Engineering, University of Panzhihua, Panzhihua 617000, China, e-mail: 25971025@qq.com

highly conductive ZrC phases *via* electrospinning and high-temperature pyrolysis [25]. When the content of ZrC was up to 10 wt%, the conductivity of the SiC/ZrC/SiZrOC hybrid nanofibers increased from 0.34 to 2.57 S/cm. For SiC/ZrC/SiZrOC hybrid nanofibers containing 7 wt% ZrC, the initial oxidation temperature was around 600°C. When the thickness of the absorber was 3 mm, the EAB was 3 GHz (8.2–11.2 GHz), and the RL_{min} was –17.5 dB at 10.3 GHz. These results indicate that the inclusion of dielectric materials can considerably improve the MAP of SiC. However, the excellent chemical properties of SiC are degraded, especially its HTS. Therefore, finding a MAM with good HTS and complex polarization mechanism is necessary.

Good electrical characteristics and high-temperature oxidation resistance are displayed by the ternary-layered compound Ti₃AlC₂ (TAC) [26,27]. TAC is a promising replacement for SiC due to these benefits. The notion that TAC has a good HTS is supported by the modest mass gain at 800°C [28]. The abundant interface and the Ti-C bond endow TAC with a high interface polarization and electronic polarization. Li et al. successfully doped TAC with Fe (xFe-TAC) through high-temperature solid-state sintering [29]. Doping has the ability to improve defect dipole polarization and considerably diversify the phase interface of TAC. They found that when the absorber thickness was $1.5 \, \text{mm}$, the RL_{min} was $-33.3 \, \text{dB}$, and the EAB was 3.9 GHz. In addition, the core-shell design based on a heterogeneous interface can adjust the complex permittivity and interface polarization mechanism, thus optimizing impedance matching [30]. It is envisaged that TAC with a core-shell structure can achieve not only an excellent MAP but also a good HTS. SiO2 can be exploited in this aspect since it has high thermo-stability, antioxidant properties, and high microwave transmittance characteristics [31]. It hardly inhibits the coupling between matrixes. On the other hand, the antioxidant Al_2O_3 also holds the potential to maintain the diffusion barrier integrity by supplying adequate environmental protection [32].

Herein the Stöber process (SP) and the sol–gel method (SGM) based on heterogeneous interface engineering were used to construct multi-core/shell $SiO_2@Al_2O_3$ nanostructures (MCSNs) *in situ* on TAC. The results show that the MCNMs with a thickness of 135–215 nm have a significant effect on the HTS and MAP of TAC. In instance, they can nearly double the initial oxidation temperature of TAC (from 400 to 800°C) and reduce the mass gain of TAC by a factor of 6.52 (from 17.44 to 2.32%). Furthermore, the EAB can be broadened by a factor of 4.7 (from 0.69 to 3.25 GHz) with a thickness of 2.0 mm, and the RL_{min} can be increased by a factor of 2.77 (from -10.68 to -29.55 dB). The results

presented in this work can serve as a guide for designing MAMs with good MAP and HTS.

2 Experimental method

2.1 Materials

The high-temperature solid-state sintering method was employed to create the TAC that was used in the current study. Figure S1 displays the comprehensive process and composition analysis. The reagents used mainly include tetraethyl orthosilicate (TEOS; $Si(OC_2H_5)_4$), aluminum nitrate (Al(NO₃)₃·9H₂O), ammonia (NH₃·H₂O), absolute ethanol (EtOH), and deionized water (H₂O). The above reagents were analytically pure and were purchased from Sinopharm Group Chemical Agent Co. Ltd.

2.2 Sample synthesis

First, a solution was made by combining 14 ml of deionized water, 56 ml of EtOH, and 2 ml of ammonia. After 5 g TAC was added to the aforementioned solution and mechanically mixed (300 rpm) for 10 min, 14.4 ml of TEOS was added and reacted for 6 h at 30°C. The reaction products were then cleaned, dried for 24 h at 80°C in a vacuum drying oven, and the resulting sample is known as TAC@SiO₂.

Next 14 ml of deionized water and 56 ml of EtOH were mixed together in a solution. $5\,\mathrm{g}$ TAC@SiO₂ and $5\,\mathrm{g}$ Al $(\mathrm{NO_3})_3$ ·9H₂O were added sequentially, and the solution was mechanically stirred for 10 min at 300 rpm. Then, ammonia water was added dropwise, so that the PH was corrected to 11. The reaction took place for 6 h at 30°C. Furthermore, the product obtained by suction filtration of the solution was repeatedly washed and dried in a vacuum drying oven for 24 h at 80°C. Finally, the dried product was placed in a tube furnace for annealing; the obtained product is named TAC@SiO₂@Al₂O₃. The annealing temperature was 800°C (heated at the rate of 10° C/min). The annealing time was 2 h, the protective gas was N₂, and the gas flow was 80 ml/min.

2.3 Characterization

The surface morphology and element distribution of the samples were observed using a Thermo Quattro S (USA) field-emission scanning electron microscope (FESEM)

equipped with an EDAX ELECT PLUS spectrometer. The working voltage was 10 kV. A FEI Tecnai G2 F20 (USA) transmission electron microscope (TEM) equipped with an energy spectrometer (Oxford 80 T) was used for the microstructure analysis and energy-dispersive spectroscopy (EDS). The acceleration voltage was 200 kV. The phase composition of the samples was analyzed using an Ultima IV (Japan) X-ray diffractometer (XRD) with a Cu K α radiation source. The scanning rate was 5°/min. X-ray photoelectron spectroscopy (XPS) measurements were carried out using a Thermo Fisher Nexsa (USA) spectrometer with a standard Al K α X-ray source (1486.7 eV). The Raman spectra were acquired using a Thermo DXR2xi (USA), and the laser wavelength was 532 nm. Thermogravimetric (TG), differential thermogravimetric (DTG), and differential scanning calorimetric (DSC) analyses were performed using an STA 449 F3 (Germany) in the temperature range of 30-1,300°C (the heating rate was 10°C/min). The electromagnetic parameters were measured using a N5230A network vector analyzer (USA) in the frequency range of 0.5-18 GHz at room temperature. The samples used for these measurements consisted of a circular workpiece with an outer diameter of 7.0 mm and an inner diameter of 3.0 mm. The samples were composed of the different TAC-based absorbents and paraffin with a mass ratio of 4:1. The dielectric dispersion, power flow, electric field strength, and power loss density of the absorbers were computed from the measured electromagnetic parameters using the CST Studio Suite 2019 program. The simulation model consisted of a square plate with a thickness of 2.0 mm. Incident electromagnetic waves (EWs) were set to transmit in the opposite direction along the z-axis. All directions were open within the boundary conditions.

3 Results and discussion

The preparation process of TAC@SiO₂@Al₂O₃ is schematically depicted in Figure 1. First, the TAC was coated with

 SiO_2 using the classical SP. In this process, the silanol groups' bonding and dangling bonds at the TAC surface change the polarity state of the substrate, causing the $TAC@SiO_2$ particles to couple together [33,34]. Second, the surface of the coupled $TAC@SiO_2$ particles was coated with materials containing Al. Furthermore, after annealing at 800° C for 2 h in N_2 , a flaky Al_2O_3 coating was formed around the linked $TAC@SiO_2$ particles; this sample is named $TAC@SiO_2@Al_2O_3$. This is the first report on the preparation of TAC coated with MCSNs using such a simple strategy.

Figure 2 displays the microscopic morphology and composition analyses of the TAC-based absorbents. This graphic demonstrates how significantly different the morphology and structure of TAC@SiO2 are from those of TAC. It can be inferred that a coupling reaction occurred between the TAC@SiO₂ particles [35]. Additionally, the TAC@SiO₂ surface is covered with rough products during the SGM and subsequent annealing process (AP), as depicted in Figure 2(c). The linked TAC@SiO₂@Al₂O₃ particles' TEM images are displayed in Figure 2(d) and (e). Amorphous SiO₂ has a thickness of around 135 nm. The thickness of the Al₂O₃ shell is in the range of 10–80 nm. According to Figure 2(f), the (107) and (103) crystal planes of TAC correspond to the crystal plane spacings of 1.8 and 1.3, respectively. The crystal plane spacing of 2.4 Å corresponds to the (140) crystal plane of Al_2O_3 , which reconfirms the presence of Al₂O₃, as shown in Figure 2(g).

The Ti, Al, C, Si, and Al element mappings for the paired TAC@SiO₂@Al₂O₃ particles are shown in Figure 2(i)–(m). The Al, Si, C, and O elements are uniformly distributed in the coupled TAC@SiO₂@Al₂O₃ particles, indicating that SiO₂ and Al₂O₃ interact to generate a homogeneous heterostructure. The defects in heterostructures can be used as polarization centers to generate a dipole polarization [36].

Figure 3(a) shows the XRD patterns of TAC, TAC@SiO₂, and TAC@SiO₂@Al₂O₃. It can be seen that the XRD pattern of TAC is made up of 11 diffraction peaks located at 9.5, 19.2, 33.7, 36.8, 39.0, 41.8, 48.5, 56.6, 61.0, 70.6, and 74.1°,

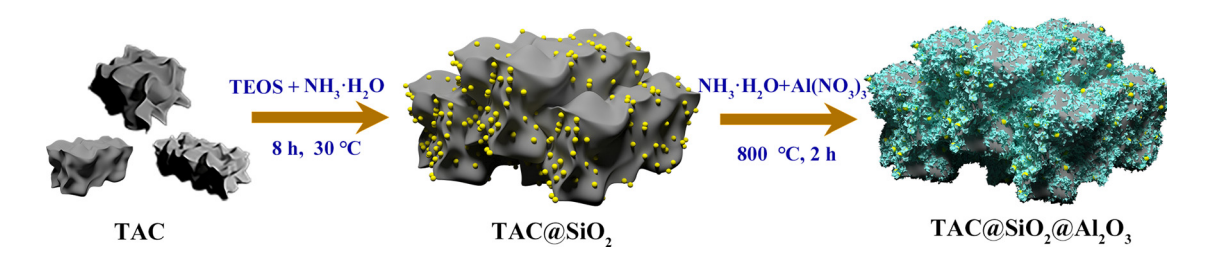


Figure 1: Schematic diagram of the synthesis process of TAC@SiO2@Al2O3.

4 — Yang Guo et al. DE GRUYTER

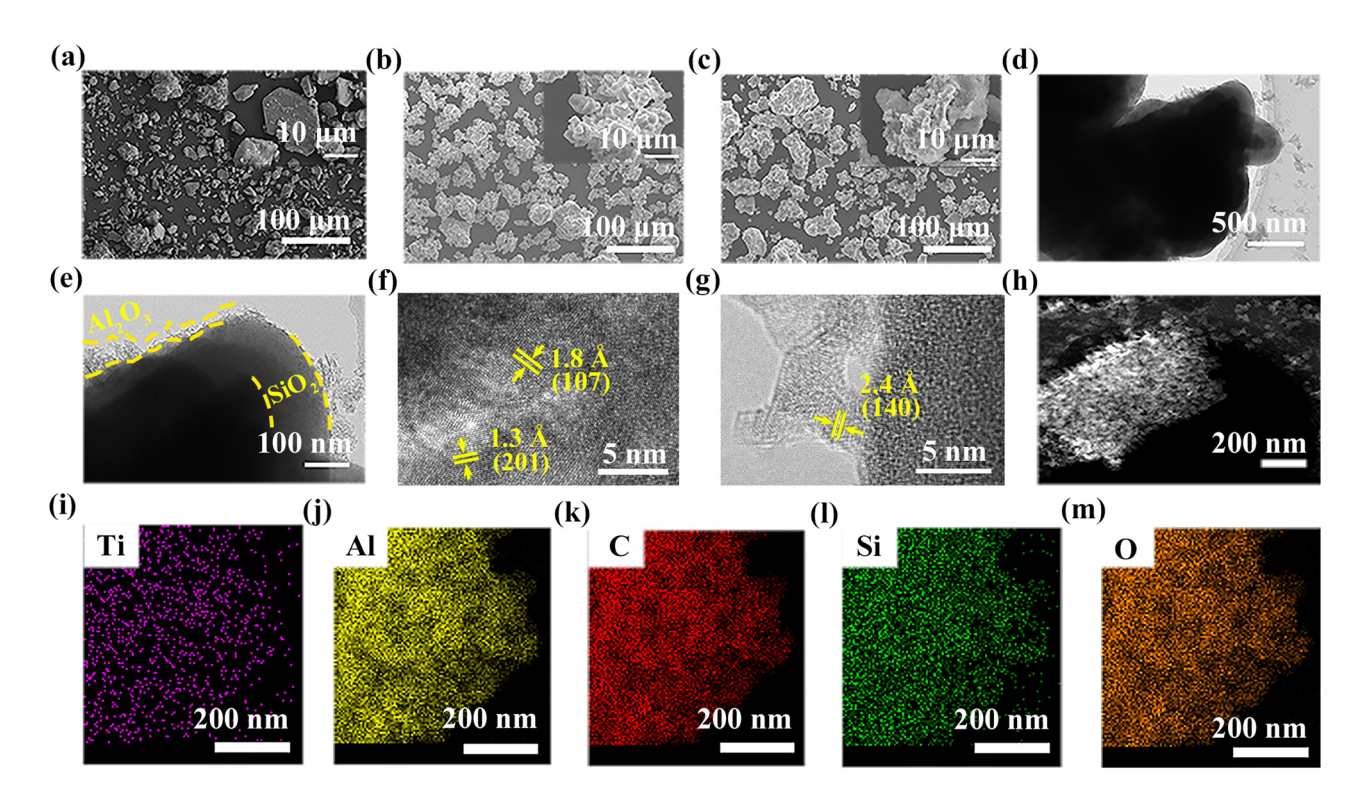


Figure 2: SEM images showing the surface appearance of (a) TAC, (b) TAC@SiO2, and (c) TAC@SiO2@Al2O3. (d) and (e) TEM images and (f) and (g) corresponding high resolution TEM images of TAC@SiO2@Al2O3. (h) TEM image of the as-fabricated TAC@SiO2@Al2O3 and corresponding elemental mapping of (i) Ti, (j) Al, (k) C, (l) Si, and (m) O.

corresponding to PDF#52-0875. After the SP, the TAC surface is coated with SiO_2 ; however, SiO_2 cannot be detected, which is mainly attributed to its amorphous state. Furthermore, after TAC@SiO₂ is subjected to the SGM and the AP, the major diffraction peaks of TAC are retained, and the Al_2O_3 diffraction peaks appear at 12.8 and 34.5°, correlating to PDF#03-0066. This shows that Al_2O_3 was successfully deposited on to the TAC surface.

The Raman shifts of TAC, TAC@SiO₂, and TAC@SiO₂@Al₂O₃ were collected in order to more precisely investigate the structure and composition of the TAC-based absorbers, as shown in Figure 3(b). The three Raman bands located at 250, 400, and 600 cm⁻¹ represent the vibration modes of the non-stoichiometric Ti-C bond in TAC. The two broad peaks located between 1,300 and 1,600 cm⁻¹ are the D and G modes of the C atom [37]. Interestingly, the Raman peaks of TAC in TAC@SiO₂@Al₂O₃ appear blue shift and move to a position with higher Raman shift, which will be caused by the high bond energy of the Si-O and Al-O bonds [38]. For TAC@SiO2, there are roughly five Raman shifts in the Raman peak corresponding to the vibration mode of the non-stoichiometric Ti-C bond. For TAC@SiO₂@Al₂O₃, the Raman peak representing the non-stoichiometric Ti-C bond experiences about 25 Raman shifts. In addition, the intensity ration of D and G (I_D/I_G) peak of TAC@SiO₂@Al₂O₃

is 1.02, which is comparable to the $I_{\rm D}/I_{\rm G}$ value of TAC@SiO₂. This shows that the MCSNs have not significantly altered the inherent state of the C atom in TAC. The findings further indicate that the MCSNs have no significant influence on the composition and structure of TAC.

Furthermore, the chemical composition and element valence state of the TAC-based absorbents were revealed via XPS, as shown in Figure 3(h)-(j). Figure 3(c) shows the high-resolution Ti 2p spectrum of TAC, which can be fitted with six peaks. The Ti $2p_{1/2}$ peak at 454.0 eV and the Ti 2p_{3/2} peak at 460.1 eV correspond to the Ti-C bond in TAC, confirming the existence of TAC [26,39]. The Ti $2p_{1/2}$ peak at 455.0 eV and the Ti 2p_{3/2} peak at 461.5 eV correspond to the Ti-O bond in non-stoichiometric TiO₂ [40]. The Ti $2p_{1/2}$ peak at 458.6 eV and the Ti $2p_{3/2}$ peak at 464.4 eV correspond to the Ti-O bond in TiO2 [41]. As shown in Figure 3(d), two peaks with binding energies of 71.8 and 74.3 eV are observed in the high-resolution Al 2p spectrum of TAC, corresponding to the Ti-Al bond in TAC and the Al-O bond in Al₂O₃, respectively [42,43]. The high-resolution C1s spectrum is fitted with four peaks (as shown in Figure 3(e)) located at 281.2, 284.8, 286.4, and 288.9 eV, corresponding to the C-Ti, C-C, C-O, and O-C=O bonds, respectively [44]. These results show that the investigated samples are mainly composed of TAC

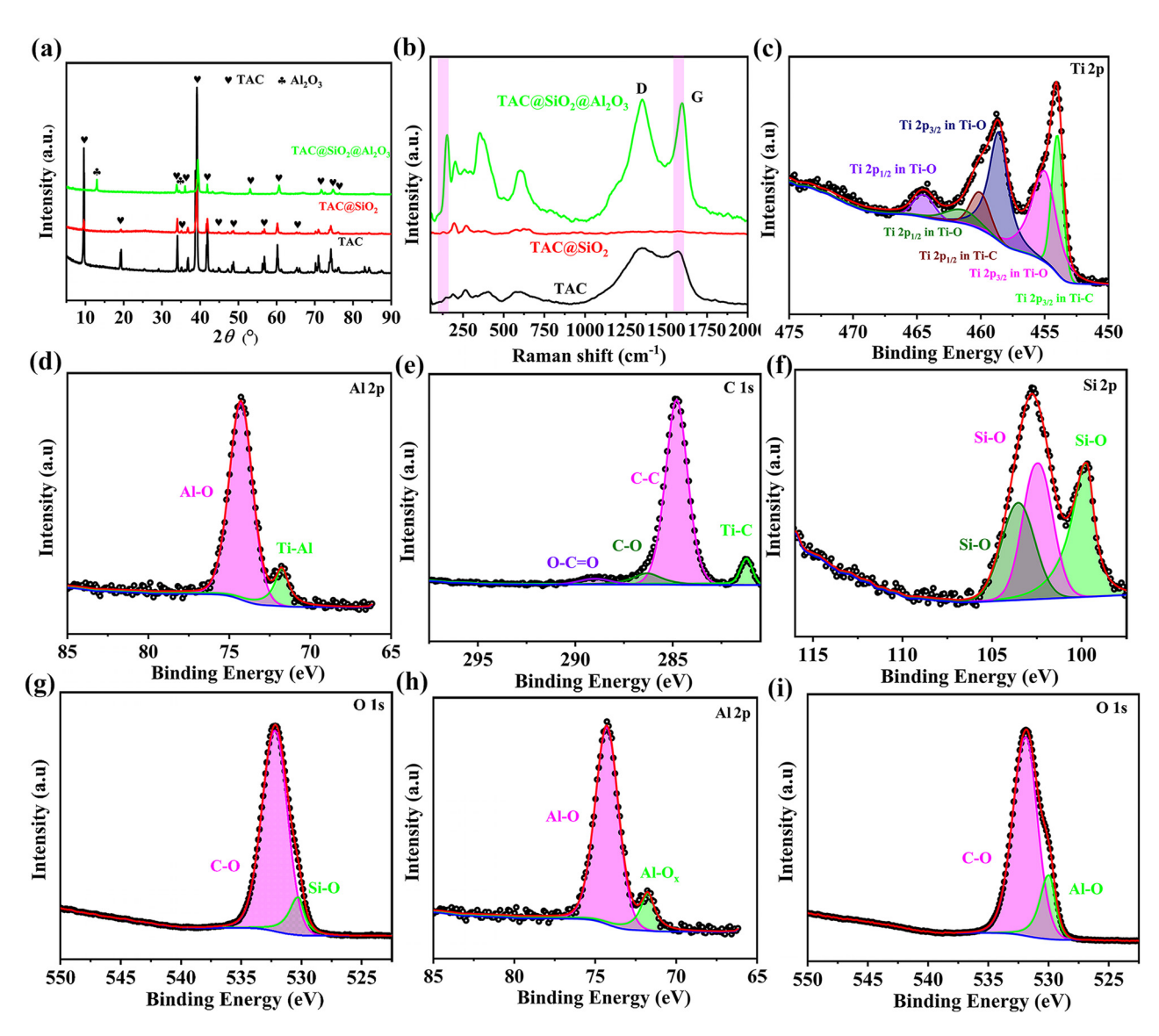


Figure 3: (a) XRD patterns of TAC, $TAC@SiO_2$, and $TAC@SiO_2@Al_2O_3$. (b) Raman spectra of TAC, $TAC@SiO_2$, and $TAC@SiO_2@Al_2O_3$. (c) High-resolution Ti 2p spectrum, (d) high-resolution Al 2p spectrum, and (e) high-resolution C 1s spectrum of TAC. (f) High-resolution Si 2p spectrum and (g) high-resolution O 1s spectrum of $TAC@SiO_2$. (h) High-resolution Al 2p spectrum and (i) high-resolution O 1s spectrum of $TAC@SiO_2@Al_2O_3$.

and contain only small amounts of TiO_2 and Al_2O_3 . Figure 3(f) and (g) show the high-resolution Si 2p and O 1s spectra of $TAC@SiO_2$. Figure 3(f) shows that the high-resolution Si 2p spectrum can be decomposed into three peaks with binding energies of 99.7, 102.4, and $103.5 \, \text{eV}$, corresponding to SiO_x (0 < x < 2), SiO_x (0 < x < 2), and SiO_2 , respectively [45–47]. The high-resolution O 1s spectrum of $TAC@SiO_2$ can be divided into two peaks located at 530.2 and 532.2 eV, as shown in Figure 3(g), corresponding to the Si–O and C–O bonds, respectively [48]. The high-resolution Si 2p and O 1s spectra of $TAC@SiO_2$ confirm the existence of SiO_2 . The position

difference in the O 1s peaks of TAC and TAC@SiO₂ is mainly caused by the C–O bond in air [49]. In the high-resolution Al 2p spectrum of TAC@SiO₂@Al₂O₃, an intense peak is observed at 75.0 eV, corresponding to Al₂O₃ [50,51], as shown in Figure 3(h), while the peak at 72.3 eV corresponds to AlO_x [52]. The appearance of Al₂O₃ is derived from the annealing of Al(OH)₃ in N₂·Al(OH)₃ is from the hydrolysis of Al₃(NO₃)₃·₉H₂O in NH₃·H₂O. The specific reaction equation is shown in equations (1) and (2).

$$Al_3(NO_3)_3 \cdot 9H_2O + 3NH_3 \cdot H_2O + 27H_2O$$

 $\rightarrow 3Al(OH)_3 \downarrow + 9NH_4NO_3,$ (1)

$$2Al(OH)_3 \rightarrow Al_2O_3 + 3H_2O.$$
 (2)

In the high-resolution O 1s spectrum of the coupled TAC@SiO₂@Al₂O₃ particles (Figure 3(i)), the peaks at 529.9 and 531.9 eV correspond to the Al–O and C–O bonds, respectively [53–55]. The above analysis results fully confirm the successful preparation of TAC@SiO₂@Al₂O₃. More importantly, the structural synergy of the three substances is the key to improve the HTS and MAP of the TAC-based absorbents.

The TG analysis can reveal the thermal stability and oxidation stability of samples at different temperatures and atmospheres. Therefore, we examined the HTS of the TAC-based absorbents from room temperature to 1,300°C, as shown in Figure 4. It is evident that all samples exhibit almost the same characteristic curves, as shown in Figure 4(a). It can be observed that the initial oxidation temperature of TAC is approximately 400°C.

The initial oxidation temperature of TAC@SiO₂ is around 500°C. Furthermore, the initial oxidation temperature of TAC@SiO₂@Al₂O₃ is up to 800°C. As demonstrated, the MSCNs raise the TAC's initial oxidation temperature by 400°C. Thus, it is clear that the MSCNs greatly enhance the HTS of TAC. It is possible mainly because of the MSCNs' ability to significantly decrease the number of transport channels connecting oxygen and TAC. SiO₂@Al₂O₃ can constitute a dense network structure [56]. This network structure can effectively reduce the number of transport channels between oxygen and the ceramic matrix and restrict oxygen diffusion to the interior, improving TAC's high-temperature oxidation resistance. Figure 4(b) shows the DTG curves of TAC, TAC@SiO2, and TAC@SiO2@Al2O3. It can be noted that the weight gain rate of TAC is 0.03%/°C. On the other hand, the weight gain rate of TAC@SiO₂@Al₂O₃ coated with the MSCNs is only 0.008%/°C. Furthermore, the

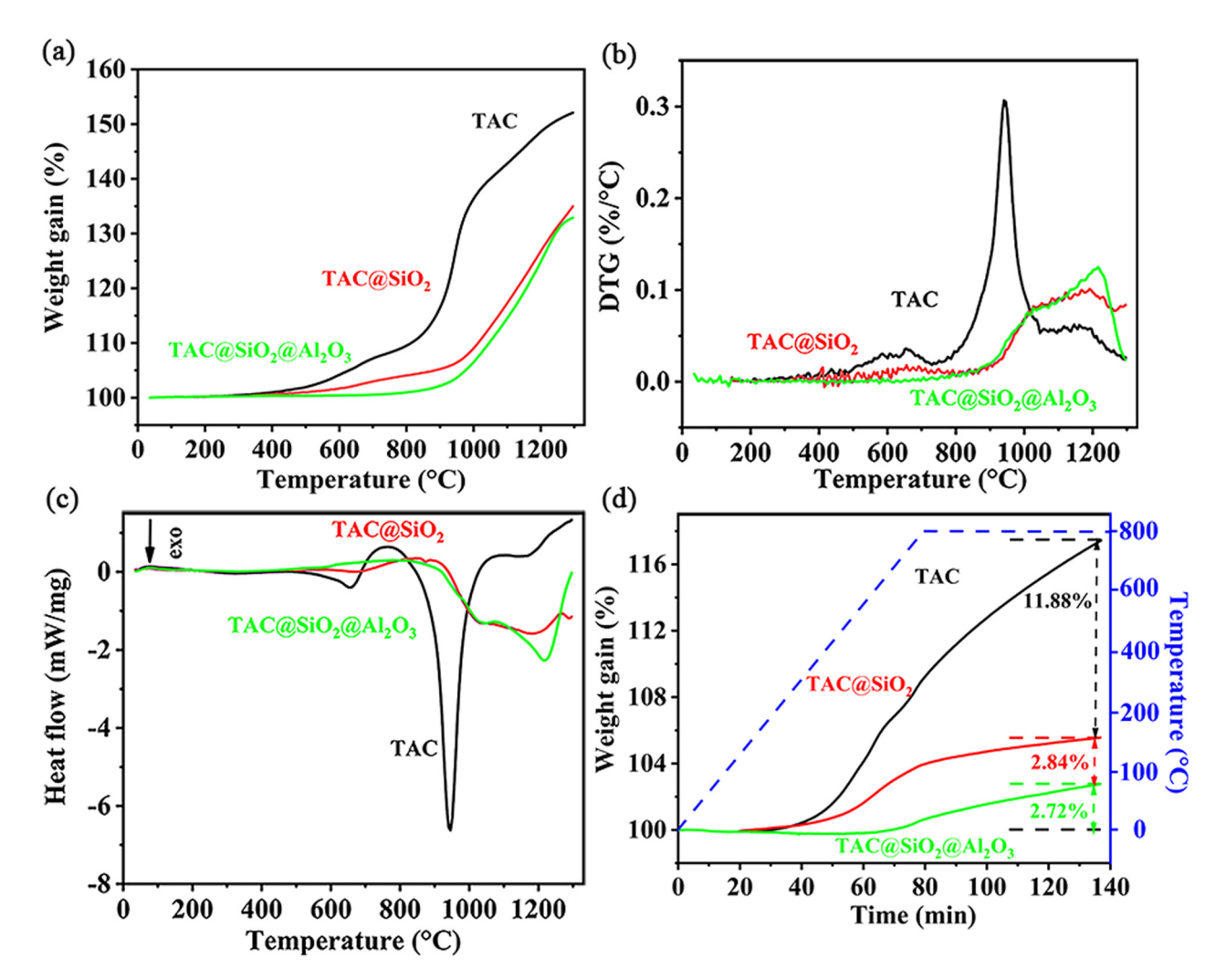


Figure 4: HTS analysis of the TAC-based absorbents at high temperature. (a) TG, (b) DTG, and (c) DSC analysis of TAC, TAC@SiO₂, and TAC@SiO₂@Al₂O₃; these curves were obtained at 800°C in air over the period of 1 h.

exothermic peaks of TAC, TAC@SiO₂, and TAC@SiO₂@Al₂O₃ are located at 944.59, 1,178, and 1,220°C, respectively, as shown in Figure 4(c). All these point to the fact that MSCN can greatly increase TAC's high-temperature oxidation resistance. The TAC-based absorbents were submitted to isothermal TG tests at 800°C in air over the course of 1 h to verify that the HTS of TAC is improved, as shown in Figure 4(d). It is obvious that TAC's mass increase can reach 14.70%, whereas TAC@SiO₂@Al₂O₃'s mass increase is just 2.72%.

To establish the MAP of MAMs, electromagnetic characteristics are crucial. As a result, we examined the real part (ε') and imaginary part (ε'') of the TAC-based absorbers as well as the dielectric loss tangent (tan δ_{ϵ}) of the complex permittivity, as shown in Figure S3. ε' represents the capacity of a material to store electric energy, while ε'' and tan δ_{ε} indicate the capacity of a material to dissipate the incident EWs. As is well known, TAC, SiO₂, and Al₂O₃ are all non-magnetic materials, and the complex permeability is thus not considered here. The ε' of TAC, TAC@SiO₂, and TAC@SiO₂@Al₂O₃ decreases with the increase in frequency, as shown in Figure S3(a) and (b). This is because the dipoles in the TAC-based absorbers rearrange when an electric field is applied. The dielectric polarization caused by the rearranged dipoles is reduced as the frequency rises, preventing them from following the electric field and causing a decrease in the dielectric response. In addition, the ε' of TAC is 15.9–18.0 in the range of 0.5–18 GHz, and the ε' of TAC coated with the MCSNs is 15.1–17.9. The ε'' of TAC is 0.007–0.33 at 0.5–18 GHz, and the ε'' of TAC@SiO₂@Al₂O₃ is 0.04–0.51. It can be seen that the ε'' of TAC@SiO₂@Al₂O₃ is significantly lower than that of TAC at 7-14 GHz. The TAC@SiO2@Al2O3 has a greater ε'' than TAC at 0.5–15 GHz. Additionally, the tan δ_{ε} values of the TAC-based absorbers were determined. It was discovered that the tan δ_{ε} of TAC@SiO₂@Al₂O₃ is higher than that of TAC in the range of 0.5-13 GHz. It is clear that TAC@SiO₂@Al₂O₃ has a greater ability than TAC to disperse incident EWs. In addition, the MAP of TAC@SiO2@Al2O3 around 11 GHz is almost unaffected by sample thickness. Two main reasons cause this: when the thickness of the absorber layer increases to a certain level, the absorption capacity of the material will reach its limit, i.e., saturation state [57]. Second, due to the particular shape and size of the TAC, there may be a resonance phenomenon at a specific frequency point [58]. That is, when the frequency of the microwave is equal to the resonance frequency of the material, the absorption performance will reach its peak.

In order to more intuitively analyze the impact of the MCSNs on the properties of the TAC, the RL values of the TAC-based absorbers were calculated using equations (3)

and (4). The 3D RL maps of the TAC-based absorbers with a thickness of 0.5-5 mm in the frequency range of 0.5-18 GHz are shown in Figure 5(a)-(c) [59,60].

$$Z_{\rm in} = Z_0 \sqrt{\frac{\mu_r}{\varepsilon_r}} \tanh \left(j \frac{2\pi f}{c} d\sqrt{\mu_r \cdot \varepsilon_r} \right), \tag{3}$$

RL = 20lg
$$\left| \frac{Z_{\text{in}} - Z_0}{Z_{\text{in}} + Z_0} \right|$$
, (4)

where $Z_{\rm in}$ and Z_0 stand for the input impedance and internal impedance, respectively. Additionally, μ_r stands for the complex permeability, ε_r represents the complex dielectric constant, f is the microwave frequency, d marks the thickness of the absorber, and c specifies the speed of light.

According to the comparisons of the RL curves of the TAC-based absorbers with a thickness of 2.0 mm at 0.5-18 GHz, it is found that the EAB of TAC is 0.69 GHz (9.75-10.44 GHz), and the RL_{min} is -10.68 dB (10.09 GHz). The EAB of TAC@SiO₂ is 1.50 GHz (9.03-9.42 GHz and 9.99–11.12 GHz), and the RL_{min} is –20.70 dB (10.39 GHz). The EAB of TAC@SiO2@Al2O3 is 3.25 GHz (8.68-11.27 and 11.63–12.29 GHz), and the RL_{min} is –29.55 dB (10.52 GHz). Compared with pure TAC, the EAB of TAC coated with MCSNs is 4.7 times higher and the RL_{min} is 2.77 times higher, demonstrating outstanding microwave absorption capabilities. This can be explained by the following two aspects: First, the multi-peak resonances induced by the heterogeneous interfaces broaden the EAB of the TAC. TAC@SiO₂@Al₂O₃ is mainly composed of TAC, amorphous SiO₂, and Al₂O₃. The four resonance peaks located at 6.64, 9.82, 12.64, and 14.56 GHz, as shown in Figure S3(b), are induced by the three-phase interactions, surface geometric enhancement effect, and local space charge accumulation [61–63]. Compared with the three resonance peaks of TAC located at 7.48, 11.38, and 13.76 GHz, both the number and intensity of the resonance peaks of TAC@SiO2@Al2O3 are higher. It is noteworthy that the resonance peak of TAC coated with the MCSNs moves to a lower frequency. This can be explained by the quarter-wavelength resonance equation $f_m = [(2k-1)c]/(4t_m n)$ [11], where f_m is the resonant frequency, t_m stands for the resonant thickness, k is a positive integer, and $n = \text{Re}(\sqrt{\varepsilon_r \mu_r})$ denotes the refractive index of the composite material. Second, the combination of the TAC and the MCSNs induces the establishment of multiple loss mechanisms. SiO_2 and Al_2O_3 are wave transmitting materials with two predominant functionalities: First, being window materials, a small amount of RL is converted into heat energy when the EWs are refracted and penetrate into the absorber. Second, given a certain amount of incident EWs, wave transmitting materials can promote more of 8 — Yang Guo et al. DE GRUYTER

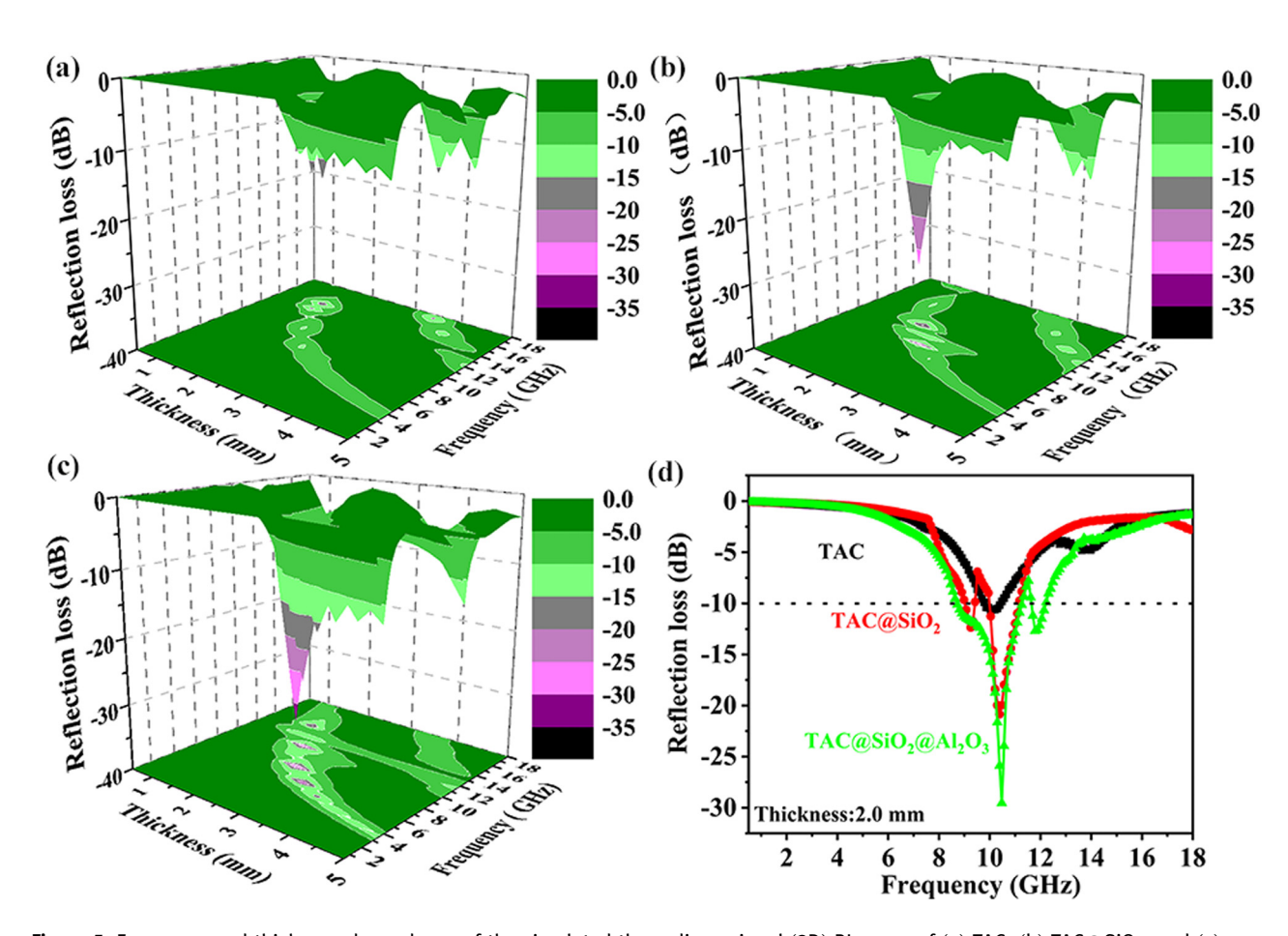


Figure 5: Frequency and thickness dependence of the simulated three-dimensional (3D) RL maps of (a) TAC, (b) TAC@SiO₂, and (c) TAC@SiO₂@Al₂O₃. (d) RL curves of the TAC-based absorbers with a thickness of 2.5 mm in the range of 0.5–18 GHz.

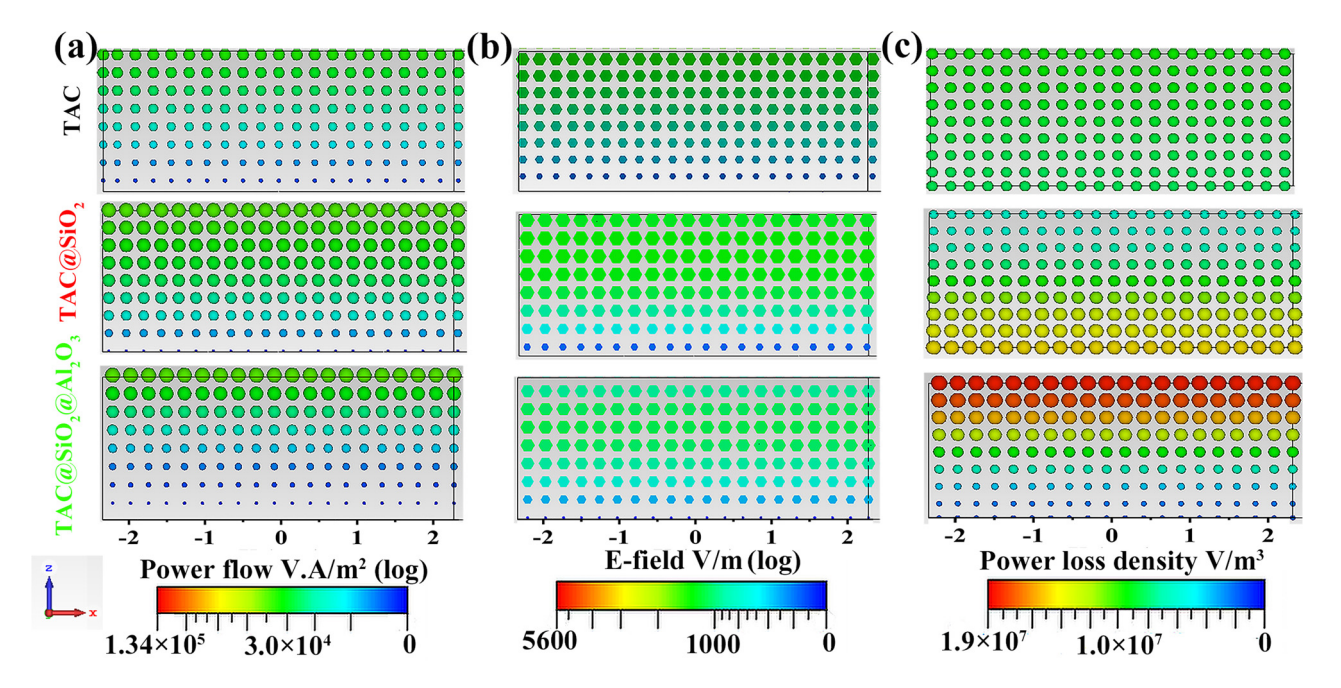


Figure 6: (a) Power flow, (b) electric field, and (c) power loss density distribution diagrams of TAC, TAC@SiO₂, and TAC@SiO₂@Al₂O₃ with a thickness of 2.0 mm at 10.48 GHz.

these EWs to penetrate into the absorber. In this process, the electronic polarization, interface polarization, and polarization relaxation generated by the conductive TAC core attenuate the incident EWs. According to the Debye relaxation theory, the main loss mechanisms of dielectric materials are polarization relaxation and conduction loss [64]. Generally, polarization relaxation and conduction loss can be studied using the Cole–Cole plots, as shown in Figure S4. ε' and ε'' can be expressed using the following equation [65,66]:

$$\left(\varepsilon' - \frac{(\varepsilon_{\rm S} + \varepsilon_{\rm co})}{2}\right)^2 + (\varepsilon'')^2 = \left(\frac{\varepsilon_{\rm S} - \varepsilon_{\rm co}}{2}\right)^2,\tag{5}$$

where ε_s denotes the static permittivity, and ε_{∞} presents the high-frequency limited permittivity.

In the Cole-Cole plot, a semicircle represents a relaxation process. The polarization relaxation loss increases with the semicircle radius. In the Cole-Cole plot, the slope of a straight line represents the strength of conductive loss. The greater the slope of the line, the stronger the conduction loss [18]. As seen in Figure S4, TAC@SiO₂@Al₂O₃ exhibits a stronger polarization loss and conduction loss than TAC. In addition, the numerous heterogeneous interfaces (such as those between TAC, amorphous SiO₂, and Al₂O₃) can heighten the interface polarization. Compared with a single TAC@SiO₂@Al₂O₃ particle, the coupling of different TAC@SiO2@Al2O3 particles gives rise to more heterogeneous interfaces, further enhancing the interfacial polarization. The existence of defect sites (such as Schottky defects and Frenkel defects) in the flaky Al₂O₃ structure and the SiO₂/Al₂O₃ heterostructure can induce the generation of a dipole polarization and an atomic polarization centered on each defect, thereby boosting the polarization relaxation [67-69]. The attenuation constants of TAC, TAC@SiO2, and TAC@SiO2@Al2O3 for incident EWs in the range of 0.5-18 GHz are shown in Figure S5. It is clear that TAC@SiO₂@Al₂O₃ has a much greater attenuation capacity than TAC for incident EWs.

In order to visually depict the positive effects of the MSCNs, the power flow $(V\cdot A/m^2)$, electric field (V/m), and power loss density (W/m^3) of the TAC-based absorbers were simulated using the CST software, as shown in Figure 6. To guarantee the validity of the result, the simulated S11 coefficient and calculated RL curves of the TAC-based absorbers were compared, as shown in Figure S6. The consistency of the S11 and RL results proves the correctness of the simulation model. The circular spots in Figure 6(a) show that the power flow of TAC@SiO2 is noticeably higher than that of TAC based on their size and color. The power flow of TAC@SiO2@Al2O3 is greater in the upper portion of the absorber than that of TAC@SiO2. The power going into TAC@SiO2@Al2O3 at the lower portion

of the absorber is less than that flowing into $TAC@SiO_2$. The high conductivity of coupled $TAC@SiO_2@Al_2O_3$, which results in a potent reflection for the incident EWs, is responsible for this phenomenon. Figure 6(b) shows the electric field (V/m) of the TAC-based absorbers. In the TAC-based absorbers, the electric field intensity decreases from top to bottom. The reduction in the electric field strength (where the electric field represents the microwaves) indicates that the loss ability for EWs of the MAMs becomes gradually stronger [70]. $TAC@SiO_2@Al_2O_3$ has a lower electric field intensity in the upper portion of the absorber than TAC and $TAC@SiO_2$. Thus, $TAC@SiO_2@Al_2O_3$ provides the best EW attenuation capability.

4 Conclusion

In this study, a simple combination of the SP and SGM based on heterogeneous interface engineering is first proposed to prepare MCSNs on TAC. The thickness of the MCSNs was roughly 145-215 nm. The HTS and MAP of TAC coated with the MSCNs are significantly enhanced. The starting oxidation temperature of TAC@SiO₂@Al₂O₃ is 800°C, which is about 400°C higher than that of TAC. After holding at 800°C for 1h, the mass gain of TAC is only 2.32%, which is 14.70% less than that of TAC. The EAB of TAC@SiO₂@Al₂O₃ is 3.25 GHz (8.68-11.27 and 11.63-12.29 GHz) at a thickness of 2.0 mm, which is 4.7 times more than that of TAC. The RL_{min} is reduced by a factor of 2.77, from -10.68 dB at 10.09 GHz to -29.55 dB at 10.52 GHz. This is because there are fewer transport pathways between oxygen and TAC as a result of MSCNs. Additionally, they increase the number of multiple reflection events, strengthen the scattering mechanism, and enhance the electronic polarization, interface polarization, and polarization relaxation. Such a simple strategy to improve the HTS and MAP of the matrix is useful in the design of MAMs with excellent MAP and HTS.

Funding information: The present study was financially supported by the National Natural Science Foundation of China (No. 52202368), the Natural Science Foundation of Sichuan (Nos. 2022NSFSC0347 and 2023NSFSC0586), the Open Projects of Vanadium and Titanium Resource Comprehensive Utilization Key Laboratory of Sichuan Province (Nos. 2021FTSZ05 and 2021FTSZ11), the Open project of Sichuan Vanadium Titanium Materials Engineering Technology Research Center (Nos. 2022FTGC01 and 2022FTGC02), and the guiding science and technology projects of Panzhihua (No. 2021ZD-G-4).

Author contributions: All authors have accepted responsibility for the entire content of this manuscript and approved its submission.

Conflict of interest: The authors state no conflict of interest.

References

- Shao G, Shen X, Huang X. Multilevel structural design and heterointerface engineering of a host-guest binary aerogel toward multifunctional broadband microwave absorption. ACS Mater Lett. 2022;4:1787-97.
- [2] Quan B, Gu W, Sheng J, Lv X, Mao Y, Liu L, et al. From intrinsic dielectric loss to geometry patterns: Dual-principles strategy for ultrabroad band microwave absorption. Nano Res. 2021;14:1495–501.
- [3] Yang G, Li Z, Haipeng L, Longjiang D. Preparation of multi-shell FeSiAl@SiO₂@C and its corrosion resistance and electromagnetic properties. Rare Met Mater Eng. 2022;51:2280-7.
- [4] Zhou N, Zhang L, Wang W, Zhang XQ, Zhang KQ, Chen MJ, et al. Stereolithographically 3D printed SiC metastructure for ultrabroadband and high temperature microwave absorption. Adv Mater Technol. 2022;2201222.
- [5] Jiang Z, Si H, Li Y, Li D, Chen H, Gong C, et al. Reduced graphene oxide@carbon sphere based metacomposites for temperature-insensitive and efficient microwave absorption. Nano Res. 2022;15:8546–54.
- [6] Ma W, He P, Wang T, Xu J, Liu X, Zhuang Q, et al. Microwave absorption of carbonization temperature-dependent uniform yolk-shell H-Fe₃O₄@C microspheres. Chem Eng J. 2021:420:129875.
- [7] Li C, Li D, Zhang L, Zhang Y, Zhang L, Gong C, et al. Boosted microwave absorption performance of transition metal doped TiN fibers at elevated temperature. Nano Res. 2023;16:3570-9.
- [8] Gu H, Huang J, Li N, Yang H, Chen G, Dong C, et al. Reactive MnO₂ template-assisted synthesis of double-shelled PPy hollow nanotubes to boost microwave absorption. J Mater Sci & Technol. 2023;146:145-53.
- [9] Wang H, Li Z, Dong B, Sun W, Yang X, Liu R, et al. Recent progresses of high-temperature microwave-absorbing materials. Nano. 2018;13:1830005.
- [10] Shi Y, Li D, Si H, Jiang Z, Li M, Gong C, et al. TiN/BN composite with excellent thermal stability for efficiency microwave absorption in wide temperature spectrum. J Mater Sci & Technol. 2022;130:249-55.
- [11] Guo Y, Jian X, Zhang L, Mu C, Yin L, Xie J, et al. Plasma-induced FeSiAl@Al₂O₃@SiO₂ core—shell structure for exceptional microwave absorption and anti-oxidation at high temperature. Chem Eng J. 2020;384:123371.
- [12] Yang X, Duan Y, Zeng Y, Pang H, Ma G, Dai X. Experimental and theoretical evidence for temperature driving an electric-magnetic complementary effect in magnetic microwave absorbing materials. J Mater Chem C. 2020;8:1583–90.
- [13] Yin P, Zhang L, Feng X, Wang J, Dai J, Tang Y. Recent progress in ferrite microwave absorbing composites. Integr Ferroelectr. 2020;211:82-101.

- [14] Qiu Y, Yang H, Wen B, Ma L, Lin Y. Facile synthesis of nickel/ carbon nanotubes hybrid derived from metal organic framework as a lightweight, strong and efficient microwave absorber. J Colloid Interface Sci. 2021;590:561–70.
- [15] Che RC, Zhi CY, Liang CY, Zhou XG. Fabrication and microwave absorption of carbon nanotubes/CoFe₂ O₄ spinel nanocomposite. Appl Phys Lett. 2006;88:033105.
- [16] Wu F, Yang K, Li Q, Shah T, Ahmad M, Zhang Q, et al. Biomass-derived 3D magnetic porous carbon fibers with a helical/chiral structure toward superior microwave absorption. Carbon. 2021;173:918–31.
- [17] Zhao Y, Zhang Y, Yang C, Cheng L. Ultralight and flexible SiC nanoparticle-decorated carbon nanofiber mats for broad-band microwave absorption. Carbon. 2021;171:474–83.
- [18] Huang B, Wang Z, Hu H, Xiu-ZhiTang, Huang X, Yue J, et al. Enhancement of the microwave absorption properties of PyC-SiC_f/SiC composites by electrophoretic deposition of SiC nanowires on SiC fibers. Ceram Int. 2020;46:9303–10.
- [19] Su J, Wang B, Cao X, Yang R, Zhao H, Zhang P, et al. Simultaneously enhancing mechanical and microwave absorption properties of C_f/SiC composites via SiC nanowires additions. Ceram Int. 2022;48:36238–48.
- [20] Meng L, Zhou Z, Xu M, Yang S, Si K, Liu L, et al. Anomalous thickness dependence of Curie temperature in air-stable twodimensional ferromagnetic 1T-CrTe₂ grown by chemical vapor deposition. Nat Commun. 2021;12:1–8.
- [21] Saroha R, Oh JH, Lee JS, Kang YC, Jeong SM, Kang DW, et al. Hierarchically porous nanofibers comprising multiple core-shell Co₃O₄@graphitic carbon nanoparticles grafted within N-doped CNTs as functional interlayers for excellent Li−S batteries. Chem Eng J. 2021;426:130805.
- [22] Zeng X, Li E, Xia G, Xie N, Shen ZY, Moskovits M, et al. Silicabased ceramics toward electromagnetic microwave absorption. J Eur Ceram Soc. 2021;41:7381–403.
- [23] Yang J, Liu X, Gong W, Wang T, Wang X, Gong R. Temperature-insensitive and enhanced microwave absorption of TiB₂/Al₂O₃/MgAl₂O₄ composites: Design, fabrication, and characterization. J Alloy Compd. 2022;894:162144.
- [24] Han T, Luo R, Cui G, Wang L. Effect of SiC nanowires on the high-temperature microwave absorption properties of SiC_f/SiC composites. J Eur Ceram Soc. 2019;39:1743–56.
- [25] Huo Y, Zhao K, Miao P, Kong J, Zhuo X, Wang K, et al. Microwave absorption performance of SiC/ZrC/SiZrOC hybrid nanofibers with enhanced high-temperature oxidation resistance. ACS Sustain Chem & Eng. 2020;8:10490-501.
- [26] Ronda-Lloret M, Yang L, Hammerton M, Marakatti VS, Tromp M, Sofer Z, et al. A. Sepúlveda-Escribano, E.V. Ramos-Fernandez, J.J. Delgado, G. Rothenberg, Molybdenum Oxide Supported on Ti₃AlC₂ is an Active Reverse. Water-Gas Shift Catalyst, ACS Sustain Chem & Eng. 2021;9:4957-66.
- [27] Quispe R, Torres C, Eggert L, Ccama GA, Kurniawan M, Hopfeld M, et al. Tribological and mechanical performance of Ti₂AlC and Ti₃AlC₂ thin films. Adv Eng Mater. 2022;24:2200188.
- [28] Drouelle E, Gauthier-Brunet V, Cormier J, Villechaise P, Sallot P, Naimi F, et al. Microstructure-oxidation resistance relationship in Ti₃AlC₂ MAX phase. J Alloy Compd. 2020;826:154062.
- [29] Li J, Xu T, Bai H, Shen Z, Huang Y, Xing W, et al. Structural modifications and electromagnetic property regulations of

- Ti₃AlC₂ MAX for enhancing microwave absorption through the strategy of Fe doping. Adv Mater Interfaces. 2022;9:2101510.
- [30] Tong Z, Liao Z, Liu Y, Ma M, Bi Y, Huang W, et al. Hierarchical Fe₃O₄/Fe@C@MoS₂ core-shell nanofibers for efficient microwave absorption. Carbon. 2021;179:646-54.
- [31] Gong X, Wang K, Dang Z, Zhang T, Xie F, Zhong B, et al. An easy multiple-layer evaporation method to prepare SiO_xC_v submicrowires with notable transmittance properties. Mater Res Bull. 2022;150:111794.
- [32] Yang P, Xiao G, Ding D, Ren Y, Yang S, Lv L, et al. Antioxidant properties of low-carbon magnesia-carbon refractories containing AlB2-Al-Al2O3 composites. Ceram Int. 2022:48:1375-81.
- [33] Liu B, Zhou H, Meng H, Pan G, Li D. Fresh properties, rheological behavior and structural evolution of cement pastes optimized using highly dispersed in situ controllably grown nano-SiO2. Cem Concr Compos. 2023;135:104828.
- [34] Montaño-Priede JL, Coelho JP, Guerrero-Martínez A, Peña-Rodríguez O, Pal U. Fabrication of monodispersed Au@SiO2 nanoparticles with highly stable silica layers by ultrasoundassisted stober method. J Phys Chem C. 2017;121:9543-51.
- [35] Sun J, Shi Z, Dai J, Song X, Hou G. Early hydration properties of Portland cement with lab-synthetic calcined stöber nano-SiO₂ particles as modifier. Cem Concr Compos. 2022;132: 104622.
- [36] Xiang Z, Wang Y, Yin X, He Q. Microwave absorption performance of porous heterogeneous SiC/SiO₂ microspheres. Chem Eng J. 2023;451:138742.
- [37] Li G, Tan L, Zhang Y, Wu B, Li L. Highly efficiently delaminated single-layered MXene nanosheets with large lateral size. Langmuir. 2017;33:9000-6.
- [38] Rakhi RB, Ahmed B, Hedhili MN, Anjum DH, Alshareef HN. Effect of postetch annealing gas composition on the structural and electrochemical properties of Ti₂CT_x MXene electrodes for supercapacitor applications. Chem Mater. 2015;27: 5314-23.
- [39] Tasleem S, Tahir M, Zakaria ZY. Fabricating structured 2D Ti₃AlC₂ MAX dispersed TiO₂ heterostructure with Ni₂P as a cocatalyst for efficient photocatalytic H2 production. J Alloy Compd. 2020;842:155752.
- [40] Li H, Cao H, Liu F, Li Y, Qi F, Ouyang X, et al. Microstructure, mechanical and electrochemical properties of Ti₃AlC₂ coatings prepared by filtered cathode vacuum arc technology. J Eur Ceram Soc. 2022;42:2073-83.
- [41] Gao Y, Wang HY, Guan J, Lan L, Zhao C, Xie LY, et al. Highvoltage arc erosion behavior and mechanism of Ti3AlC2 under different ambient atmospheres. J Eur Ceram Soc. 2021;41:2263-77.
- [42] Chen J, Cheng J, Li F, Zhu S, Li W, Yang J, et al. Tribological study on a novel wear-resistant $AlMgB_{14}$ -Si composite. Ceram Int. 2017;43:12362-71.
- [43] Liu X, Chen W, Zhang X. Ti₃AlC₂/Pd composites for efficient hydrogen production from alkaline formaldehyde solutions. Nanomaterials. 2022;12:843.
- [44] Cao M, Wang F, Wang L, Wu W, Lv W, Zhu J. Room temperature oxidation of Ti₃C₂ MXene for supercapacitor electrodes. J Electrochem Soc. 2017;164:A3933-42.
- [45] Ryaguzov A, Kudabayeva M, Myrzabekova M, Nemkayeva R, Guseinov N. Influence of Si atoms on the structure and

- electronic properties of amorphous DLC films. J Non-Crystalline Solids. 2023;599:121956.
- [46] Hu D, Lu J, Deng J, Yan Q, Long H, Luo Y. The polishing properties of magnetorheological-elastomer polishing pad based on the heterogeneous Fenton reaction of single-crystal SiC. Precis Eng. 2023;79:78-85.
- [47] Sun H, Xi Y, Tao Y, Zhang J. Facile fabrication of multifunctional transparent glass with superhydrophobic, self-cleaning and ultraviolet-shielding properties via polymer coatings. Prog Org Coat. 2021;158:106360.
- [48] Ferreira-Neto EP, Ullah S, Martinez VP, Yabarrena J, Simões MB, Perissinotto AP, et al. Thermally stable SiO₂@TiO₂ core@shell nanoparticles for application in photocatalytic self-cleaning ceramic tiles. Mater Adv. 2021;2:2085-96.
- [49] Cao M, Zhao X, Gong X. Ionic liquid-assisted fast synthesis of carbon dots with strong fluorescence and their tunable multicolor emission. Small. 2022;18:2106683.
- [50] Kong X, Li Z, Zhao X, Chen XP, Wu ZY, He F, et al. Surface group directed low-temperature synthesis and self-assembly of Al nanostructures for lithium storage. Nano Res. 2023:16:1733-9.
- [51] Kobayashi Y, Tada S, Kikuchi R. Porous intermetallic Ni₂XAl (X= Ti or Zr) nanoparticles prepared from oxide precursors. Nanoscale Adv. 2021;3:1901-5.
- [52] Hoque E, DeRose JA, Hoffmann P, Mathieu HJ, Bhushan B, Cichomski M. Phosphonate self-assembled monolayers on aluminum surfaces. J Chem Phys. 2006;124:174710.
- Huang S, Li X, Zhao Y, Sun Q, Huang H. A novel lapping process [53] for single-crystal sapphire using hybrid nanoparticle suspensions. Int J Mech Sci. 2021;191:106099.
- [54] Deng Z, Liang J, Liu Q, Ma C, Xie L, Yue L, et al. High-efficiency ammonia electrosynthesis on self-supported Co₂AlO₄ nanoarray in neutral media by selective reduction of nitrate. Chem Eng J. 2022;435:135104.
- [55] Pan L, Jiang K, Zhai G, Ji H, Li N, Zhu J, et al. A novel 2D conjugated coordination framework with a narrow bandgap for micro-supercapacitors. Energy Technol. 2022;10:
- [56] Lutpi HA, Mohamad H, Abdullah TK, Ismail H. Effect of ZnO on the structural, physio-mechanical properties and thermal shock resistance of Li₂O-Al₂O₃-SiO₂ glass-ceramics. Ceram Int. 2022;48:7677-86.
- [57] Jiang D, Yang Y, Huang C, Huang M, Chen J, Rao T, et al. Removal of the heavy metal ion nickel (II) via an adsorption method using flower globular magnesium hydroxide. J Hazard Mater. 2019;373:131-40.
- [58] Pan J, Guo H, Wang M, Yang H, Hu H, Liu P, et al. Shape anisotropic Fe₃O₄ nanotubes for efficient microwave absorption. Nano Res. 2020;13:621-9.
- Xiao J, Qi X, Wang L, Jing T, Yang JL, Gong X, et al. Anion regulating endows core@shell structured hollow carbon spheres@MoS_xSe_{2-x} with tunable and boosted microwave absorption performance. Nano Res. 2023;16:1-11.
- [60] Sun H, Che R, You X, Jiang Y, Yang Z, Deng J, et al. Crossstacking aligned carbon-nanotube films to tune microwave absorption frequencies and increase absorption intensities. Adv Mater. 2014;26:8120-5.
- [61] Guo Y, Zhang L, Lu H, Jian X. In situ regulation of microstructure and microwave-absorbing properties of FeSiAl through HNO₃ oxidation. Nanotechnol Rev. 2022;11:147-57.

- [62] Sun Z, Yan Z, Guo Z, Liu H, Zhao L, Qian L. A synergistic route of heterointerface and metal single-atom configurations towards enhancing microwave absorption. Chem Eng J. 2023;452:139430.
- [63] Wu Z, Cheng HW, Jin C, Yang B, Xu C, Pei K, et al. Dimensional design and core-shell engineering of nanomaterials for electromagnetic wave absorption. Adv Mater. 2022;34:2107538.
- [64] Dai YL, Guo AP, Gong MH, Zhang XJ, Wen BY. Rational design of heterointerface between MoO₂ and N-doped carbon with tunable electromagnetic interference shielding capacity. J Colloid Interface Sci. 2023;636(15):492-500.
- [65] Yang N, Luo ZX, Wu G, Wang YZ. Superhydrophobic hierarchical hollow carbon microspheres for microwave-absorbing and self-cleaning two-in-one applications. Chem Eng J. 2023;454:140132.
- [66] Che RC, Peng LM, Duan XF, Chen Q, Liang X. Microwave absorption enhancement and complex permittivity and per-

- meability of Fe encapsulated within carbon nanotubes. Adv Mater. 2004;16:401-5.
- [67] Gao Z, Song Y, Zhang S, Lan D, Zhao Z, Wang Z, et al. Electromagnetic absorbers with Schottky contacts derived from interfacial ligand exchanging metal-organic frameworks. J Colloid Interface Sci. 2021;600:288–98.
- [68] Liu Q, Cao Q, Bi H, Liang C, Yuan K, She W, et al. CoNi@SiO₂@TiO₂ and CoNi@Air@TiO₂ microspheres with strong wideband microwave absorption. Adv Mater. 2016;28:486–90.
- [69] Rao L, Wang L, Yang C, Zhang R, Zhang J, Liang C, et al. Confined diffusion strategy for customizing magnetic coupling spaces to enhance low-frequency electromagnetic wave absorption. Adv Funct Mater. 2023;33:2213258.
- [70] Ning M, Kuang B, Wang L, Li J, Jin H. Correlating the gradient nitrogen doping and electromagnetic wave absorption of graphene at gigahertz. J Alloy Compd. 2021;854:157113.